PCCP

RSC Publishing

PAPER

View Article Online
View Journal | View Issue

Cite this: *Phys. Chem. Chem. Phys.*, 2013, **15**, 17165

Wrinkled-graphene enriched MoO_3 nanobelts with increased conductivity and reduced stress for enhanced electrochemical performance

Yifan Dong, Shuo Li, Hongmei Xu,* Mengyu Yan, Xiaoming Xu, Xiaocong Tian, Qing Liu and Liqiang Mai*

Received 1st August 2013,
Accepted 9th August 2013

DOI: 10.1039/c3cp53267d

www.rsc.org/pccp

MoO_3 has long suffered from poor conductivity and cyclability, which limit its high rate performance and ultralong cycling ability. Increasing the electronic conductivity with electron pathways of cathode materials can effectively enhance the lithium storage properties with stable cyclability and rate capability theoretically. Here the MoO_3–reduced graphene oxide (rGO) hybrid nanobelts were designed and prepared and were tested as cathode materials for lithium batteries. It is demonstrated that the rGO is wrinkled and twisted around MoO_3 nanobelts after reacting under high temperature and pressure conditions. The unique morphology of rGO, which has continuous electron pathways and stress buffering effects, endows the MoO_3–rGO hybrid nanobelts with significantly increased rate capability and cycling ability. Meanwhile, it is demonstrated that MoO_3–rGO hybrid nanobelts are promising cathode materials for use in rechargeable lithium batteries and our synthesis strategy is also versatile for exploiting advanced materials for Li-ion batteries.

Introduction

With the growing demand for energy, exploring new energy storage systems to overcome the shortcomings of the ordinary fuel energy storage is a challenge nowadays.[1–8] Rechargeable lithium batteries have attracted a lot of attentions because of their low cost, long cycle life, high energy density and good reversibility.[9–13]

There are numerous candidates for the Li-ion battery electrode materials such as layered, spinel, polyoxyanionic and olivine structured compounds. Among the transition-metal oxides, MoO_3 has been extensively investigated as a key material for fundamental researches and technological applications in optical devices,[14] field-emission-devices,[15] catalysts,[16] sensors,[17,18] and lubricants[19] with its unique layered structure and moderate band gap. Especially in electrochemical storage application, MoO_3 is a promising candidate because of its stability, high theoretical capacity and facility for scaling up.[20] Starting from α-MoO_3 as the precursor, many novel nanomaterials have been synthesized such as nanowires, nanoplatelets, nanobelts and nanorods.[21–23]

Nevertheless, MoO_3 is still facing some limitations such as low-conductivity and structure-degradation issues, which lead to poor kinetics and/or a serious capacity fading during cycling, especially at higher rates.[24,25] Hu *et al.* have investigated the electrical conductivity of an individual MoO_3 nanobelt, and found that the conductivity is 3 orders of magnitude lower than that of a single MoO_2 nanorod which is commonly used as anode.[26] Mai *et al.* have assembled a single nanowire device to measure the electrical transport through a single MoO_3 nanowire before and after lithiation, and the conductivity is evaluated to increase from 10^{-4} S cm^{-1} before lithiation to 10^{-2} S cm^{-1} after lithiation, but at the expense of the fractures and breaks in MoO_3 nanowires.[27] Therefore, increasing the conductivity and relieving the structure degradation effectively in MoO_3 nanobelts are efficient ways to increase their rate performance as well as cycling stability in electrochemical applications. It is reported that graphene, a single layer of sp^2-bonded carbon atoms tightly packed into a two-dimensional honeycomb structure with excellent mobility of charge carriers (200 000 cm^2 V^2 s^{-1}) and electrons (15 000 cm^2 V^{-1} cm^{-1}) and a high value of stiffness of 130 Gpa,[28,29] is a promising candidate for metal oxide–graphene nanocomposites to overcome the limitations of metal oxides.[30–35]

Until recently, the effective synthesis of MoO_3–graphene composites with excellent electrochemical performance has been rarely reported due to the fact that the intrinsic limitations of low conductivity and large irreversible capacity of MoO_3 are difficult to be overcome by simply mixing MoO_3 with graphene,[36–39] and the high-rate performance and long cycle life of MoO_3 in lithium ion batteries are also hard to achieve. Importantly, Noerochim *et al.* reported that graphene could act as a buffer layer during

State Key Laboratory of Advanced Technology for Materials Synthesis and Processing, WUT-Harvard Joint Nano Key Laboratory, Wuhan University of Technology, Wuhan, 430070, P. R. China. E-mail: mlq518@whut.edu.cn, xhm790912@163.com; Fax: +86-27-87644867; Tel: +86-27-87467595

cycling even after 100 cycles of Li^+ insertion–extraction and MoO_3–graphene hybrid materials with improved performances were attained.[34] Here we have designed and successfully synthesized bonded MoO_3–rGO hybrid nanobelt composites by employing a facile hydrothermal method. The MoO_3 nanobelts are uniform in structure with rGO twisting and wrinkling around them. The wrinkled rGO provides high-conductive electron pathways between MoO_3 nanobelts, and additionally it alleviates the nanobelt degradation during cycling as rGO relieves the stress during lithium intercalation and deintercalation. Our results show that by rGO wrinkling, the electrochemical performance of MoO_3 nanobelts has been significantly increased, which has resulted in a prolonged cycle life of 500 cycles and ultrahigh rate performance.

Experimental

Synthesis of MoO_3–rGO hybrid nanobelts

Firstly, rGO was prepared by a modified Hummer's method with additional $KMnO_4$.[40] The graphite (1 g) was mixed with 23 mL of concentrated sulfuric acid in a 250 mL beaker and stirred at room temperature for 24 hours. Then the flask was placed in a water bath at 40 °C and 100 mg of $NaNO_3$ was added to the suspension and allowed to dissolve for 5 minutes. This step was followed by slow addition of 500 mg of $KMnO_4$, keeping the temperature below 45 °C. The solution was stirred for 30 minutes. Next, 3 mL of water was added to the beaker, followed by another 3 mL after 5 minutes. In another 5 minutes, 40 mL of water was added. 15 minutes later, the beaker was removed from the water bath and 140 mL of water and 10 mL of 30% H_2O_2 were added to end the reaction. The suspension was then repeatedly centrifuged and washed twice with 5% HCl solution and then repeatedly with water. The collected precipitate was dispersed in 100 mL of water and bath sonicated for 60 min. After being centrifuged at 5000 rpm, a brown homogeneous supernatant was obtained. To prepare the MoO_3–rGO hybrid nanobelts, 40 mL of H_2O_2 (30%) was agitated rapidly, and 4 g of molybdenum powder was added slowly under water-cooling until the clear orange peroxomolybdic acid sol was obtained, and then 5 mL of as-prepared rGO was added into 30 mL of sol in a 70 °C water bath for 4 h, and transferred into a Teflon lined autoclave afterwards and kept at 180 °C for 6 h. The autoclave was left to cool, and the precipitate was filtered out and rinsed with deionized water three times.

Material characterization

X-ray diffraction (XRD) measurements were performed to investigate the crystallographic information using a Bruker D8 Advance X-ray diffractometer with a non-monochromated Cu Kα X-ray source. Raman spectra were acquired using a Renishaw RM-1000 laser Raman microscopy system. Scanning electron microscopy (SEM) images were collected using a JEOL JSM-7100F at an acceleration voltage of 15 kV. Transmission electron microscopic (TEM) and high resolution transmission electron microscopic (HRTEM) images were recorded using a JEOL JEM-2100F STEM/EDS microscope. The atomic force microscopic (AFM) image was recorded using a Bruker MultiMode 8 Atomic Force Microscope.

Electrochemical measurements

The electrochemical properties were characterized in coin cells using lithium metal foil as the anode. The cathode electrodes were composed of 70% active material, 20% acetylene black and 10% poly(tetrafluoroethylene) (PTFE) binder. The specific capacity is calculated by multiplying a factor of 0.7 to calculate the active materials of MoO_3–rGO. The carbon black is used as a dispersing agent and a conducting additive to ensure the successful grinding of the as-prepared powders to cut into pellets. A solution (1 M) of $LiPF_6$ in EC–DEC (1 : 1 vol/vol) was used as the electrolyte. The cells were assembled in an argon-filled glove-box. Galvanostatic charge–discharge measurements were performed using a multichannel battery testing system (LAND CT2001A), cyclic voltammetry (CV) and electrochemical impedance spectroscopy (EIS) were performed using an Autolab Potentiostat Galvanostat. All the measurements were carried out at room temperature.

Results and discussions

The synthetic route for preparation of MoO_3–rGO hybrid nanobelts is shown in Fig. 1. One of the advantages of the as-synthesized graphene oxide is the presence of many oxygen-containing functional groups on its edges and surface. When rGO is added into the peroxomolybdic acid sol, whose structural formula is $Mo_4(O)_{12}(O_2)_2H_2O_4^{4-}$, the functional groups on rGO and in peroxomolybdic acid sol (such as HO–C═O and −OH) will have interfacial interactions by reactive chemisorption that bridge metal centers with carboxyl or hydroxyl groups at oxygen-defect sites, and van der Waals interactions between the pristine region of graphene and metal oxides.[41] The subsequent stirring and heating will accelerate this process and seed crystals of MoO_3 will grow and bond with rGO.

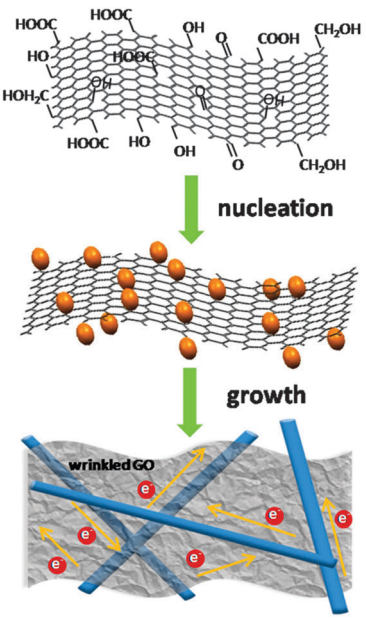

Fig. 1 Schematic illustration of the synthetic route for preparation of MoO_3–rGO hybrid nanobelts.

The energy release along the [001] direction of MoO_3 is greater than that of the other crystal orientations, thus the growth of MoO_3 along the [001] direction is preferred and can grow into nanobelt morphology. As the MoO_3 nanobelts begin to grow in an autoclave at high pressure and temperature, the rGO attached with the MoO_3 seed crystals suffers the stress which is derived from the nanobelts growth. With the simultaneous extreme environment, the rGO has the trend to twist and wrinkle around MoO_3 nanobelts, forming the MoO_3–rGO hybrid nanobelts.[42] This rational design utilizes both the advantages of rGO (superior electrical conductivity and structural flexibility) and MoO_3 (large capacity and high energy density) to alleviate the insufficiencies of rGO (re-stacking during cycling and large irreversible capacity, *etc.*) and MoO_3 (poor electrical conductivity, large volume change, severe aggregation/agglomeration, poor rate capability and cycling stability, *etc.*). Therefore, this structure possesses the synergistic effects of rGO and MoO_3 and can effectively suppress the agglomeration of MoO_3 nanobelts and re-stacking of graphene. Additionally, rGO forms a highly conducting and flexible network which ensures the fast kinetics of lithium diffusion and electron transport, thus the electrode performance can be significantly enhanced.

Fig. 2a shows the X-ray diffraction (XRD) pattern of the MoO_3–GO hybrid nanobelt product. All the diffraction peaks can be assigned to a pure orthorhombic phase of MoO_3 (JCPDS No. 89-5108; a = 3.9620 Å, b = 13.8550 Å, and c = 3.7010 Å). No characteristic peaks of rGO were observed, due to the strong intensities of the diffraction peaks from crystalline MoO_3 nanostructures and the small quantity of rGO. The Raman spectrum of MoO_3–rGO hybrid nanobelts is shown in Fig. 2b. The presence of the D and G bands confirms the presence of rGO. The D band located at 1330 cm^{-1} is mainly due to the sp^3 hybridized C–C bonds. The G band appears at 1590 cm^{-1} is due to the sp^2 hybridized C–C bonds in a two-dimensional hexagonal lattice.[43] It can be observed from the inset of Fig. 2b that the D/G ratio of rGO in the hybrid nanomaterial is 1.06, slightly higher than 0.86 for pure as-synthesized rGO, indicating that some extra functional groups containing oxygen were formed on rGO after hydrothermal reaction with MoO_3. This observation further shows that there are bonds between MoO_3 nanobelts and rGO. The Raman spectrum of the MoO_3–rGO hybrid nanobelts also shows three sharp characteristic bands of MoO_3. The peak at 996 cm^{-1} is assigned to the vibration of $\nu Mo{=}O_{(1)}$, and the peak at 820 cm^{-1} can be assigned to the asymmetrical and symmetrical stretching vibrations of the $Mo_{(3)}$–O–$Mo_{(3')}$ bonds, while the band at 664 and 472 cm^{-1} can be attributed to the asymmetrical stretching vibration of $O_{(2,2)}Mo_3$ bonds. The peaks located at 302 cm^{-1}, 270 cm^{-1} and 246 cm^{-1} can be attributed to the vibrations of δMoO_3, $\delta Mo{=}O$ and δOMo_2. Peaks observed in the range of 100–200 cm^{-1} correspond to various bending modes of the α-MoO_3 crystal. These observations correspond well to the previously published literature.[34]

The morphology and thickness of rGO are observed under AFM (Fig. 3a) after sonication. The average thickness is 0.7 nm, indicating the monolayers of as-synthesized rGO. As shown in Fig. 3b, the SEM image of MoO_3–rGO hybrid nanobelts exhibits the combination of wrinkled rGO and uniform MoO_3 nanobelts, the widths of MoO_3 nanobelts are in the range of 200–300 nm and the MoO_3 nanobelts are intertwined by rGO. TEM and HRTEM images (Fig. 3c and d) reveal further information about the morphology and structure of the MoO_3–rGO hybrid nanobelts. The rGO shows a typical wrinkled morphology in the TEM image and the MoO_3 nanobelts are overlapped and surrounded by rGO. The HRTEM image shows the typical MoO_3 lattice fringes of the as-synthesized MoO_3–rGO hybrid nanobelts. The periodic fringe spacings of ~3.80 and ~3.26 Å agree well with the interplanar spacings of the (110) and (021) planes of orthorhombic MoO_3, respectively. The SAED (Fig. 3d inset) image reveals that the MoO_3 nanobelts are single-crystalline.

To characterize the electrochemical properties of MoO_3–rGO hybrid nanobelts, CV results of pure MoO_3 and MoO_3–rGO hybrid nanobelts are shown in Fig. 4a. The voltammograms were measured at a sweep rate of 0.1 mV s^{-1} in the potential range from 4.0 to 1.5 V *vs.* Li/Li^+ at room temperature. It is obvious that MoO_3–rGO hybrid

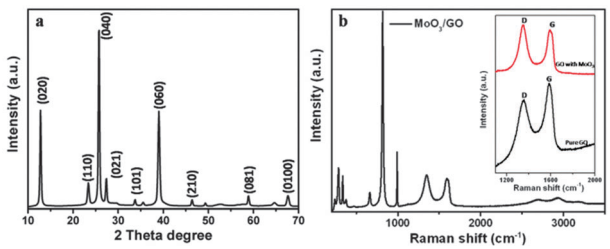

Fig. 2 (a) X-ray diffraction patterns of MoO_3–rGO hybrid nanobelts. (b) Raman spectra of MoO_3–rGO hybrid nanobelts (inset: comparison of D and G bands of rGO before and after reacting with MoO_3).

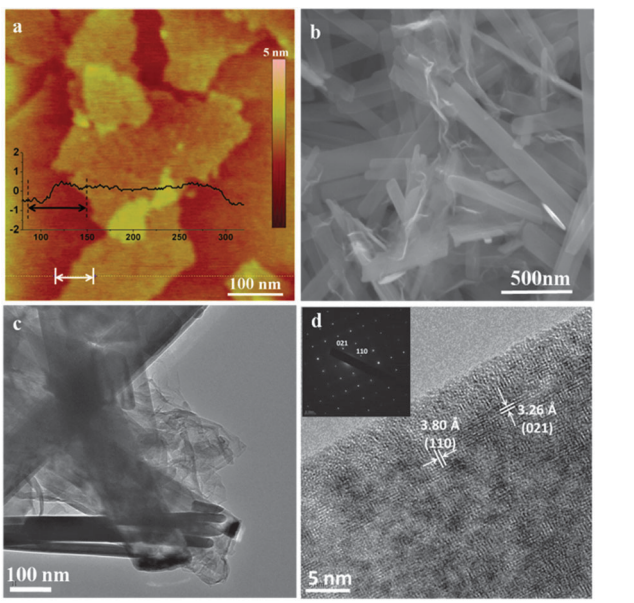

Fig. 3 Morphologies of rGO and MoO_3–rGO hybrid nanobelts (a) AFM image of rGO. (b) The SEM image of MoO_3–rGO hybrid nanobelts. (c) The TEM image of MoO_3–rGO hybrid nanobelts. (d) The HRTEM image and the electron diffraction pattern (inset) of MoO_3–rGO hybrid nanobelts.

nanobelts have a larger curve area and a higher redox peak current than pure MoO_3, suggesting that MoO_3–rGO hybrid nanobelts have the higher capacity and the faster kinetics for Li-ion insertion–extraction. The cathodic peaks located at around 2.6 and 2.17 V are obtained from both samples during the negative scan. These two reduction peaks correspond to two consecutive Li intercalations into the electrode. The 2.6 V cathodic peak can be assigned to the irreversible lithium insertion into the crystal structure (the intralayers of $[MoO_6]$), which tends to cause unrecoverable structure transformation of MoO_3. The anodic peak located at 2.53 V for both the pure MoO_3 nanobelts and the MoO_3–rGO hybrid nanobelts during the positive scan corresponds to the reversible insertion of lithium ions into the interlayer spacings (van der Waals spacings) between the $[MoO_6]$ octahedron layers. Fig. 4b shows the discharge and charge curves of the MoO_3–rGO hybrid nanobelts at the current densities of 0.5 to 2 A g^{-1}. The discharge capacities are 289, 238 and 138 mA h g^{-1} at the current densities of 0.5, 1 and 2 A g^{-1}, respectively. The discharge and the charge curves have two voltage plateaus due to Li^+ intercalation into the electrode, which is consistent with the results on cathodic and anodic peak potentials in the cyclic voltammograms.

Electrochemical impedance spectroscopy (EIS) measurements were used to compare the resistance of the prepared MoO_3 and MoO_3–rGO hybrid nanobelts (Fig. 4c). The impedance measurements were performed after 10 cycles of charge–discharge at a potential of 2 V *vs.* Li/Li^+ to ensure the stable interfaces in the electrode. It can be seen clearly that the R_{ct} of MoO_3–rGO hybrid nanobelt electrode is much lower than that of the MoO_3 nanobelt electrode, which indicates that the graphene twisting could enable much easier charge transfer at the electrode/electrolyte interface and consequently decrease the overall battery internal resistance.

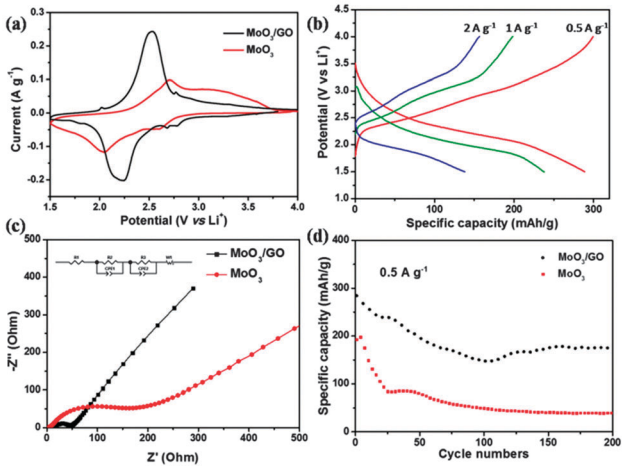

Fig. 4 Electrochemical properties of pure MoO_3 and MoO_3–rGO hybrid nanobelts. (a) Cyclic voltammetry (CV) curves at a sweep rate of 0.1 mV s^{-1} in the potential range from 4.0 to 1.5 V *vs.* Li/Li^+. (b) The initial charge–discharge curves of MoO_3–rGO hybrid nanobelts at the current densities of 0.5, 1 and 2 A g^{-1}, respectively. (c) Electrochemical impedance spectra of the pure MoO_3 nanobelts and the MoO_3–rGO hybrid nanobelt electrode. (d) The cycling performance of pure MoO_3 nanobelts and MoO_3–rGO hybrid nanobelts at the current density of 0.5 A g^{-1}.

The diffusion coefficient values of the lithium ions (D) can be calculated using the equation $D = 0.5(RT/AF^2\sigma_w C)^2$, where R is the gas constant, T is the temperature, A is the area of the electrode surface, F is Faraday's constant, and C is the molar concentration of Li^+ ions. The calculated lithium diffusion coefficient values for pure MoO_3 nanobelts and MoO_3–rGO hybrid nanobelts are 7.8×10^{-12} and 3.7×10^{-11} cm^2 s^{-1}, respectively. It can be seen that the lithium diffusion coefficient of MoO_3–rGO hybrid nanobelts is about one order of magnitude larger than that of pure MoO_3 nanobelts.

The comparison of cycling performance of the MoO_3–rGO hybrid nanobelts at 0.5 A g^{-1} with pure MoO_3 nanobelts in the voltage range of 1.5–4 V is demonstrated in Fig. 4d. The MoO_3–rGO hybrid nanobelt electrode shows a higher capacity and better cycling performance. The initial discharge capacity of MoO_3–rGO hybrid nanobelts is 289 mA h g^{-1}, while for pure MoO_3 nanobelts the capacity of 201 mA h g^{-1} is much lower. This is because the diffusion ability of lithium into the pure MoO_3 nanobelts is much worse than that of the MoO_3–rGO hybrid nanobelts with the enhanced conductivity by adding rGO. Therefore the initial capacity of MoO_3–rGO hybrid nanobelts is higher than that of the pure MoO_3 nanobelts, which illustrates the advantages of attaching graphene. After 200 cycles, the capacity of MoO_3–rGO hybrid nanobelts can be maintained at 174 mA h g^{-1} with the capacity retention of 61%, while for pure MoO_3 the capacity is only 38 mA h g^{-1} and the retention is only 19% after 200 cycles. Moreover, the capacity of MoO_3–rGO hybrid nanobelts slightly increases after 100 cycles. Note that the intercalation–deintercalation process of MoO_3 is an activation process: the lithium intercalates into the interlayers and intralayers of MoO_3, while the lithium in the intralayers cannot be extracted, thus leading to the irreversible capacity decrease in the first 100 cycles. As the lithium-ions accumulate in MoO_3, the conductivity and diffusion coefficient of lithium-ions in MoO_3 have increased,[27] and the increased diffusion ability of lithium makes lithium-ions intercalating into the interlayers of MoO_3 more facile, thus leading to a gradual increase of capacity.

To further evaluate the high rate performance, the cycling performance of the MoO_3–rGO hybrid nanobelts at 1 A g^{-1} is shown in Fig. 5a. The initial capacity is 238 mA h g^{-1}. After 500 cycles, the capacity can be maintained at 129 mA h g^{-1}. It can be observed that the capacity fades rapidly during the initial 30 cycles. This may be attributed to the irreversible lithium insertion into the crystal structure (the intralayers of $[MoO_6]$) at 2.6 V as indicated in the CV curve. From the 30th cycle to the 100th cycle, the MoO_3–rGO hybrid nanobelts have a significant capacity retention of 97%; from the 30th cycle to the 500th cycle, the capacity retention can still reach up to 85% with the columbic efficiency of approximately 100% in the overall cycles.

The rate performance of the pure MoO_3 nanobelts and MoO_3–rGO hybrid nanobelts at increasing current densities of 0.2 to 5 A g^{-1} is shown in Fig. 5b. The hybrid nanobelts show a much better rate performance than MoO_3. The MoO_3–rGO hybrid nanobelts deliver the discharge capacity of 225, 209, 185 and 137 mA h g^{-1} at the current densities of 0.2, 0.5, 1 and 2 A g^{-1}, respectively. At a very high current density of 5 A g^{-1},

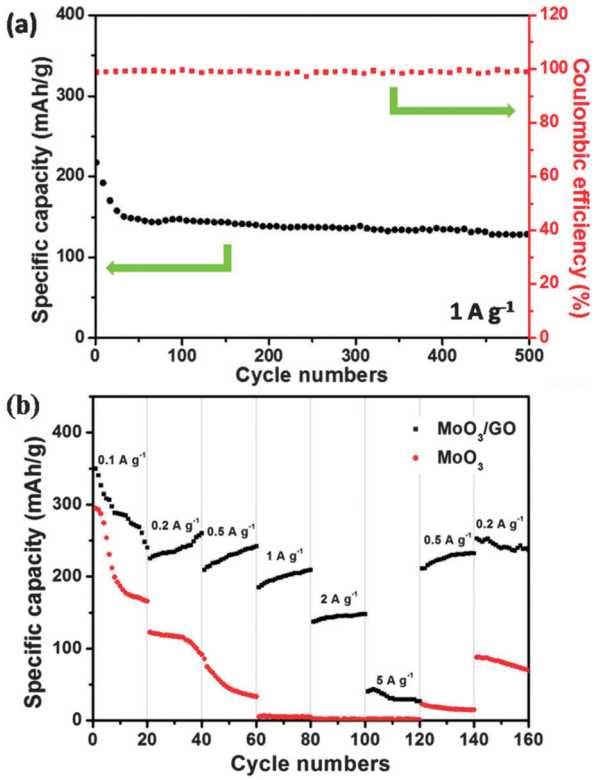

Fig. 5 (a) Cycling performance at the current density of 1 A g^{-1}. (b) Discharge capacities of pure MoO_3 and the MoO_3–rGO hybrid nanobelt cathode at various current densities from 0.2 to 5 A g^{-1}.

which is equal to 160 C in rate performance (1 C corresponds to full lithiation per hour), the capacity can still be maintained at 43 mA h g^{-1}, which is rarely reported for MoO_3 as a cathode. For pure MoO_3 nanobelts there are hardly any capacities when the current density goes up to 1 A g^{-1}. Additionally, at relatively low current densities (0.2, 0.5, 1 and 2 A g^{-1}) the capacity has the trend to rise for MoO_3–rGO hybrid nanobelts, while for MoO_3 nanobelts the capacity drops significantly at all current densities.

The excellent rate performance is because the conductivity of MoO_3–rGO is significantly enhanced by the rGO twisting. The rGO possesses a much higher conductivity than MoO_3, and forms conductive networks for electron pathways during charge–discharge. The pure MoO_3 nanobelts cannot tolerate the rapid charge–discharge rate beyond 1 A g^{-1}, while after rGO twisting, the considerable capacity can be attained even at 5 A g^{-1}. Additionally, the cycling performance has increased largely compared to pure MoO_3 nanobelts, and can maintain an excellent capacity retention of 97% from 30 to 100 cycles and 85% from 30 to 500 cycles at 1 A g^{-1}, which is rarely reported for MoO_3 as a cathode material. This may be attributed to the fact that rGO provides a faster kinetics for lithium diffusion. As observed in the AFM image of rGO, the as-synthesized rGO is flat and two-dimensional, while in SEM and TEM images of MoO_3–rGO hybrid nanobelts, the rGO is wrinkled and twisted around MoO_3 nanobelts, this structure can effectively buffer the structure degradation and volume expansion of pure MoO_3, thus promoting the cycling performance.

In our design, the wrinkled and twisted rGO after hydrothermal reaction around MoO_3 nanobelts provides continuous electron pathways which increase rate performance, and acts as a stress buffer for material degradation during lithium intercalation–deintercalation, which promotes the cycling stability.

Conclusions

By rationally controlling the rGO morphology *via* hydrothermal reaction, the MoO_3 nanobelts are wrinkled and twisted with rGO by functional group bonds and van der Waals interactions. This structure utilizes the advantages of the rGO with high-conductivity and structural-flexibility, and MoO_3 nanobelts with large capacity and good one-dimensional morphology. This synergistic effect endows this hybrid material with excellent rate performance as high as 160 C with considerable capacity and impressive cycling stability of 85% from 30 to 500 cycles at 1 A g^{-1}. The rational design of the continuous network with increased conductivity and reduced stress makes MoO_3–rGO hybrid nanobelts a promising candidate for electrode materials in Li-ion batteries and this synthetic method may lead to the development of new nanostructures with stable and high-performance materials for energy storage.

Acknowledgements

This work was supported by the National Basic Research Program of China (2013CB934103, 2012CB933003), the National Natural Science Foundation of China (51272197, 51072153), the Program for New Century Excellent Talents in University (NCET-10-0661), the International S&T Cooperation (2013DFA50840), and the Independent Innovation Research Fund in WHUT (2012-II-001, 2013-ZD-7, 2013-VII-028).

Notes and references

1 T. J. Kempa, R. W. Day, S. K. Kim, H. G. Park and C. M. Lieber, *Energy Environ. Sci.*, 2013, **6**, 719–733.
2 T. A. Faunce, W. Lubitz, A. B. Rutherford, D. MacFarlane, G. F. Moore, P. Yang, D. G. Nocera, T. A. Moore, D. H. Gregory and S. Fukuzumi, *Energy Environ. Sci.*, 2013, **6**, 695–698.
3 S. Xu, Y. Qin, C. Xu, Y. Wei, R. Yang and Z. L. Wang, *Nat. Nanotechnol.*, 2010, **5**, 366–373.
4 C. Xu and Z. L. Wang, *Adv. Mater.*, 2011, **23**, 873–877.
5 S. Chu and A. Majumdar, *Nature*, 2012, **488**, 294–303.
6 Z. Peng, S. A. Freunberger, Y. Chen and P. G. Bruce, *Science*, 2012, **337**, 563–566.
7 L. Li, S. Chen, X. Wang, Y. Bando and D. Golberg, *Energy Environ. Sci.*, 2012, **5**, 6040–6046.
8 L. Q. Mai, L. Xu, C. Han, X. Xu, Y. Luo, S. Zhao and Y. Zhao, *Nano Lett.*, 2010, **10**, 4750–4755.
9 J. M. Tarascon and M. Armand, *Nature*, 2001, **414**, 359–367.
10 L. Q. Mai, Y. Dong, L. Xu and C. Han, *Nano Lett.*, 2010, **10**, 4273–4278.
11 B. Kang and G. Ceder, *Nature*, 2009, **458**, 190–193.
12 M. Armand and J.-M. Tarascon, *Nature*, 2008, **451**, 652–657.

13 X. Xu, Y. Z. Luo, L. Q. Mai, Y. L. Zhao, Q. Y. An, L. Xu, F. Hu, L. Zhang and Q. J. Zhang, *NPG Asia Mater.*, 2012, **4**, e20.
14 Y. J. Lee, J. Yi, G. F. Gao, H. Koerner, K. Park, J. Wang, K. Luo, R. A. Vaia and J. W. Hsu, *Adv. Energy Mater.*, 2012, **2**, 1193–1197.
15 S. Balendhran, J. Deng, J. Z. Ou, S. Walia, J. Scott, J. Tang, K. L. Wang, M. R. Field, S. Russo and S. Zhuiykov, *Adv. Mater.*, 2013, **25**, 109–114.
16 T. Prasomsri, T. Nimmanwudipong and Y. Roman, *Energy Environ. Sci.*, 2013, **6**, 1732–1738, DOI: 10.1039/C3EE24360E.
17 A. Prasad, D. Kubinski and P. Gouma, *Sens. Actuators,. A*, 2003, **93**, 25–30.
18 A. M. Taurino, A. Forleo, L. Francioso, P. Siciliano, M. Stalder and R. Nesper, *Appl. Phys. Lett.*, 2006, **88**, 152111.
19 J. Wang, K. C. Rose and C. M. Lieber, *J. Phys. Chem. B*, 1999, **103**, 8405–8409.
20 Y. Sun, J. Wang, B. Zhao, R. Cai, R. Ran and Z. Shao, *J. Mater. Chem. A*, 2013, **1**, 4736–4746.
21 L. Q. Mai, F. Yang, Y. Zhao, X. Xu, L. Xu, B. Hu, Y. Luo and H. Liu, *Mater. Today*, 2011, **14**, 346–353.
22 H. B. Wu, J. S. Chen, H. H. Hng and X. W. D. Lou, *Nanoscale*, 2012, **4**, 2526–2542.
23 T. Zhai, L. Li, Y. Ma, M. Liao, X. Wang, X. Fang, J. Yao, Y. Bando and D. Golberg, *Chem. Soc. Rev.*, 2011, **40**, 2986–3004.
24 L. Zhou, L. Yang, P. Yuan, J. Zou, Y. Wu and C. Yu, *J. Phys. Chem. C*, 2010, **114**, 21868–21872.
25 S. Li, C. H. Han, L. Q. Mai, J. H. Han, X. Xu and Y. Q. Zhu, *Int. J. Electrochem. Sci*, 2011, **6**, 4504–4513.
26 B. Hu, L. Q. Mai, W. Chen and F. Yang, *ACS Nano*, 2009, **3**, 478–482.
27 L. Q. Mai, B. Hu, W. Chen, Y. Qi, C. Lao, R. Yang, Y. Dai and Z. L. Wang, *Adv. Mater.*, 2007, **19**, 3712–3716.
28 A. K. Geim and K. S. Novoselov, *Nat. Mater.*, 2007, **6**, 183–191.
29 Q. Tang, Z. Zhou and Z. F. Chen, *Nanoscale*, 2013, **5**, 4541–4583.
30 T. N. Lambert, D. J. Davis, W. Lu, S. J. Limmer, P. G. Kotula, A. Thuli, M. Hungate, G. Ruan, Z. Jin and J. M. Tour, *Chem. Commun.*, 2012, **48**, 7931–7933.
31 C. Han, M. Yan, L. Q. Mai, X. Tian, L. Xu, X. Xu, Q. An, Y. Zhao, X. Ma and J. Xie, *Nano Energy*, 2013, DOI: 10.1016/j.nanoen.2013.03.012.
32 X. Wang, X. Cao, L. Bourgeois, H. Guan, S. Chen, Y. Zhong, D. M. Tang, H. Li, T. Zhai and L. Li, *Adv. Funct. Mater.*, 2012, **22**, 2682–2690.
33 X. Huang, K. Qian, J. Yang, J. Zhang, L. Li, C. Yu and D. Zhao, *Adv. Mater.*, 2012, **24**, 4419–4423.
34 L. Noerochim, J. Z. Wang, D. Wexler, Z. Chao and H. K. Liu, *J. Power Sources*, 2013, **228**, 198–205.
35 Y. Fang, Y. Lv, R. Che, H. Wu, X. Zhang, D. Gu, G. Zheng and D. Zhao, *J. Am. Chem. Soc.*, 2013, **135**, 1524–1530.
36 F. Xia, X. Hu, Y. Sun, W. Luo and Y. Huang, *Nanoscale*, 2012, **4**, 4707–4711.
37 J. Hu, A. Ramadan, F. Luo, B. Qi, X. Deng and J. Chen, *J. Mater. Chem.*, 2011, **21**, 15009–15014.
38 T. Tao, A. M. Glushenkov, C. Zhang, H. Zhang, D. Zhou, Z. Guo, H. K. Liu, Q. Chen, H. Hu and Y. Chen, *J. Mater. Chem.*, 2011, **21**, 9350–9355.
39 X. F. Yang, H. Y. Ding, D. Zhang, X. H. Yan, C. Y. Lu, J. L. Qin, R. X. Zhang, H. Tang and H. J. Song, *Cryst. Res. Technol.*, 2011, **46**, 1195–1201.
40 D. C. Marcano, D. V. Kosynkin, J. M. Berlin, A. Sinitskii, Z. Sun, A. Slesarev, L. B. Alemany, W. Lu and J. M. Tour, *ACS Nano*, 2010, **4**, 4806–4814.
41 Z.-S. Wu, G. Zhou, L.-C. Yin, W. Ren, F. Li and H. M. Cheng, *Nano Energy*, 2012, **1**, 107–131.
42 J. Zang, S. Ryu, N. Pugno, Q. Wang, Q. Tu, M. J. Buehler and X. Zhao, *Nat. Mater.*, 2013, **12**, 321–325.
43 A. Ferrari, J. Meyer, V. Scardaci, C. Casiraghi, M. Lazzeri, F. Mauri, S. Piscanec, D. Jiang, K. Novoselov and S. Roth, *Phys. Rev. Lett.*, 2006, **97**, 187401.

